photonics

MDPI

Article

Misalignment-Induced Aberration Compensation for Off-Axis Reflective Telescopes Based on Fusion of Spot Images and Zernike Coefficients

Wei Tang [1,2,3,†], Yujia Liu [1,3,†], Weihua Tang [1,2,3], Jie Fu [1,2,3], Siheng Tian [1,2] and Yongmei Huang [1,2,*]

[1] State Key Laboratory of Optical Field Manipulation Science and Technology, Institute of Optics and Electronics, Chinese Academy of Sciences, Chengdu 610209, China
[2] Key Laboratory of Optical Engineering, Chinese Academy of Sciences, Chengdu 610209, China
[3] University of Chinese Academy of Sciences, Beijing 100049, China
* Correspondence: huangym@ioe.ac.cn
† These authors contributed equally to this work.

Abstract

Off-axis reflective telescopes are prone to component misalignment due to external environmental factors and mechanical vibrations. This misalignment introduces low-order aberrations, which severely degrade imaging quality. Thus, active misalignment correction is crucial for maintaining the imaging performance of off-axis reflective telescopes. Current computer-aided alignment technologies for optical systems mostly rely on wavefront sensors to acquire aberrations at multiple fixed fields of view (FOVs) or even the full FOV. This significantly increases system complexity and hinders practical engineering applications. To address this issue, this study first conducts sensitivity analysis of misaligned degrees of freedom (DOFs) using a mode truncation algorithm based on singular value decomposition (SVD). A compensation strategy is proposed to avoid the aberration coupling effect. Furthermore, two novel misalignment aberration compensation methods for off-axis reflective telescopes are presented. These methods require only a single focal spot image and eliminate the need for aberration detection and iterative calculations. One method directly solves component misalignment errors using a convolutional neural network (CNN) based on the system's point spread function (PSF). To further improve compensation performance, an improved method fusing spot images and Zernike coefficients is proposed. In practical misalignment correction, both methods input a single acquired focal spot image into a well-trained model to obtain the misalignment compensation amount. Simulation experiments demonstrate that the improved method, which uses Zernike polynomial coefficients as an intermediate feature bridge, effectively establishes the mapping relationship between spot images and misalignment amounts. It achieves higher solution accuracy and better aberration compensation effect compared to the direct CNN method. This verifies the necessity of extracting Zernike polynomial coefficient features from spot images. Comparative experiments with the traditional sensitivity matrix method show that the two proposed methods outperform the sensitivity matrix method in aberration compensation accuracy over a large misalignment range. Comprehensive simulation results confirm the feasibility and effectiveness of the proposed methods. They overcome the limitations of existing methods, such as complex structure, high cost, and low efficiency, to a certain extent.

Keywords: off-axis reflective telescope; misalignment; aberration compensation; spot image; zernike coefficients; convolutional neural network

Check for updates

Received: 19 January 2026
Revised: 11 February 2026
Accepted: 15 February 2026
Published: 23 February 2026

Copyright: © 2026 by the authors. Licensee MDPI, Basel, Switzerland. This article is an open access article distributed under the terms and conditions of the Creative Commons Attribution (CC BY) license.

1. Introduction

Off-axis reflective telescopes have no central obstruction. Among them, off-axis two-mirror telescopes offer advantages such as a small number of reflective surfaces, a low primary mirror F-number, and a large aperture. However, this design makes the system extremely sensitive to mirrors spatial position misalignment errors. The beam expander system, precisely aligned during the assembly phase, is subjected to wind loads, temperature changes, and mechanical vibrations during transportation and operation. Additionally, adjusting the optical axis and secondary mirror (SM) position when observing targets causes deformation of the internal mechanical structure. These factors lead to deviations in mirrors spatial positions, ultimately degrading system imaging quality. With the development of optical design and processing technology, the alignment accuracy before telescope delivery and the misalignment correction accuracy during service have become key factors limiting the final imaging quality of off-axis telescope systems [1,2]. Therefore, developing a fast and high-precision misalignment error correction method is critical for improving telescope imaging performance.

Current mainstream misalignment correction methods based on wavefront detection fall into two categories. The first category is analytical methods based on nodal aberration theory (NAT). Researchers such as Gu et al. [3], Zhang et al. [4,5], Wen et al. [6], and Bai et al. [7,8] analyzed the aberration compensation characteristics of off-axis two-mirror and three-mirror telescopes using NAT and proposed corresponding misalignment correction models. These studies provide a theoretical basis for analyzing the changes of system wavefront aberration and PSF caused by mirrors misalignment. However, the complex establishment of analytical models hinders their engineering application. The second category is alignment technology that constructs simple numerical models based on existing misalignment values and corresponding wavefront aberration coefficients using a fitting approach, also known as computer-aided alignment. Researchers such as Figoski [9], Seonghui Kim [10], and Lee [11] conducted optical system alignment research using the sensitivity matrix method, merit function regression method, and differential wavefront sampling method, respectively. The sensitivity matrix method lacks sufficient nonlinear mapping for large misalignment ranges. The merit function regression method is prone to local optima. The differential wavefront sampling method suffers from large measurement errors in practical detection. In contrast, artificial neural networks have been applied due to their strong nonlinear fitting capabilities [12,13]. It should be noted that all the above methods require additional optical equipment, such as Shack–Hartmann wavefront sensors [14], curvature sensors [15], and interferometers [16], to detect system wavefront aberration. Complex algorithms are then used to solve for misalignment values. This not only increases system complexity but also easily causes error propagation. He et al. proposed a residual-error-aware Shack–Hartmann calibration method [17], which further confirms the impact of residual errors from additional detection equipment, highlighting the necessity of sensor-free methods. Moreover, wavefront sensors are unavailable in some application scenarios, such as space telescopes, limiting the applicability of these methods.

To break this limitation, advances in wavefront sensing technology have promoted the development of methods for directly extracting Zernike polynomial coefficient features from spot images [18]. In traditional methods, phase retrieval (PR) and phase diversity (PD) infer wavefront aberrations by analyzing intensity distributions on single or multiple planes to extract coefficients; multi-channel diffractive optical element (DOE) filtering based on Zernike matching achieves coefficient separation by directly responding to specific orders of Zernike modes through customized filter structures. Notably, stray light and parameter fluctuations in optical systems can interfere with spot image quality. Zhou et al. confirmed through research on LiDAR optical systems that internal stray light

suppression [19] and adaptive parameter adjustment [20] can effectively reduce the impact of system defects, which is consistent with the idea of avoiding stray light issues through sensor-free design in this paper. With the development of deep learning, methods for directly learning the mapping relationship between focal spot morphology and Zernike coefficients using neural networks have emerged. Jiang et al.'s research [21] verified the effectiveness of deep learning-assisted phase processing, and Li et al.'s multi-stage learning strategy [22] achieved high-precision phase unwrapping under strong speckle noise, further improving the accuracy and robustness of wavefront coefficient extraction.After obtaining precise wavefront coefficients, such methods can calculate misalignment errors through the analytical and numerical approaches presented in the previous subsection. Since the principles of the above methods indicate that the image information of an optical system can reflect the magnitude of wavefront aberrations, it is also possible to directly estimate the misalignment state based on this information. Consequently, a class of methods has emerged that directly perform misalignment aberration correction using image sensors. Researchers such as Li [23] and Bai [24] used specific optimization algorithms to find the extremum of the objective function constructed from light intensity information acquired by detectors, achieving wavefront aberration compensation. However, such nonlinear optimization algorithms face difficulties in convergence and are prone to local extrema when errors are large. Additionally, multiple iterations require repeated adjustment of component positions using actuators, reducing the stability of the optical system and shortening the mechanical lifespan of optical components. In recent years, with the development of artificial intelligence technology, deep learning methods have been gradually applied to misalignment error detection, significantly reducing hardware costs and improving alignment efficiency. Researchers such as Jia et al. [25], Gu et al. [26], Bingdao Li et al. [27], and Wang et al. [28] used CNNs to fit the nonlinear relationship between defocus PSFs at different FOVs and mirrors position errors. This enabled the detection of SM position errors in coaxial reflecting space telescope (CRST) systems. However, these methods are mainly designed for misaligned coaxial reflective systems. Due to lack of rotational symmetry, off-axis reflective systems are extremely sensitive to component position errors, and aberrations introduced by different misaligned DOFs are coupled. This greatly increases the difficulty of constructing neural network models. Furthermore, extracting defocus spot images requires translating the image plane using a high-precision focusing mechanism, which increases system complexity. In summary, although existing methods have achieved certain results in telescope misalignment error detection, each has inherent limitations.

Therefore, before establishing the mapping relationship between focal spot images and misalignment values based on neural networks, this study first conducts sensitivity analysis of the SM misaligned DOFs of off-axis two-mirror telescopes using an SVD-based mode truncation algorithm [29]. A compensation strategy is proposed to avoid the multiple-solution problem in the mapping from focal spot images to misalignment values. Two novel misalignment aberration compensation methods for off-axis telescopes based on focal spot images and without the need for multiple iterations are then presented. The first method directly establishes a mathematical model between focal spot images and misalignment values using a CNN model. This method is abbreviated as CNN in Section 4. The second method, considering that traditional alignment methods accurately solve component misalignment values by acquiring Zernike polynomial coefficients and the strong nonlinear fitting capability of artificial neural networks, proposes a misalignment aberration compensation method fusing focal spot images and Zernike polynomial coefficients. This method is abbreviated as CNN-FCNN in Section 4. Network model training consists of two parts. The first part constructs a mathematical model between spot images and Zernike polynomial coefficients based on CNN. The second part fits the nonlinear mapping

relationship between Zernike polynomial coefficients and misalignment values using a fully connected neural network (FCNN). After training, the weights of the two parts are combined to form a complete new model. In practical misalignment correction, both methods input a single focal spot image of the misaligned system into the well-trained model to solve for the mirrors misalignment compensation amount in one step.

The structure of this paper is as follows. Section 2 introduces the wavefront aberration characteristics of a misaligned off-axis optical system based on NAT, and establishes the analytical relationship among the point spread function (PSF), wavefront aberrations, and misalignment using Fourier optics. Section 3 first conducts a qualitative analysis of the fact that the multi-valued inverse problem in the mapping from focal spot images to misalignment stems from the aberration coupling effect induced by different misaligned DOFs. It then applies a mode truncation algorithm based on Singular Value Decomposition (SVD) to conduct a sensitivity analysis of misaligned DOFs and proposes an aberration compensation strategy. Subsequently, the detailed implementation process of a misalignment aberration compensation method for an off-axis telescope based on fusion of focal spot images and Zernike coefficients is introduced. Section 4 validates the superiority of the proposed improved method through comprehensive simulation experiments, evaluating both misalignment estimation accuracy and wavefront correction performance. Finally, Section 5 provides a summary of the content presented in this paper.

2. Principle of the Misalignment-Induced Aberration Compensation Method Based on Fusion of Spot Images and Zernike Coefficients

2.1. Low-Order Wavefront Aberration Formula of Misaligned Off-Axis Reflective Optical Systems Based on Nodal Aberration Theory

According to nodal aberration theory, the aberration on the image plane of an optical system is the sum of aberration contributions from each surface (component). The wavefront aberration of an off-axis reflective telescope system is expressed as:

$$W = \sum_{j}\sum_{p}^{\infty}\sum_{n}^{\infty}\sum_{m}^{\infty}(W_{klm})_j(\vec{H}\cdot\vec{H})^p[(\vec{\rho}+\vec{s})\cdot(\vec{\rho}+\vec{s})]^n[\vec{H}\cdot(\vec{\rho}+\vec{s})]^m \quad (1)$$

where $(W_{klm})_j$ represents different types of wavefront aberration coefficients of the j-th surface (component) of the optical system. $\vec{H}$, $\vec{\rho}$, and $\vec{s}$ denote the normalized image-space FOV vector, pupil aperture vector, and pupil decenter vector, respectively. Notably, when $\vec{s} = 0$, the formula can represent the wavefront aberration of a coaxial system. p, n, and m represent the exponents of their vector operations, with $k = 2p + m$ and $l = 2n + m$.

Aberration analysis of off-axis reflective optical systems requires the use of a pupil coordinate transformation matrix. Introduce the pupil scaling factor B and pupil off-axis vector $\vec{d}$, i.e., $\vec{\rho}' = B\vec{\rho} + \vec{d}$. Substitute them into Equation (1) to obtain the vector expression of the aberration of the off-axis reflective optical system:

$$W = \sum_{j}\sum_{p}^{\infty}\sum_{n}^{\infty}\sum_{m}^{\infty}(W_{klm})_j(\vec{H}\cdot\vec{H})^p[(B\vec{\rho}+\vec{d})\cdot(B\vec{\rho}+\vec{d})]^n[\vec{H}\cdot(B\vec{\rho}+\vec{d})]^m \quad (2)$$

When component misalignment exists, the wavefront aberration of the full FOV changes accordingly. To characterize the influence of component misalignment values on system wavefront aberration, a normalized aberration field decenter vector $\vec{\sigma}_j$ is introduced to represent the offset vector of the aberration center of the j-th surface relative to that of the ideal system. Based on this offset vector, the effective FOV in the misaligned state is expressed as $\vec{H}_{Aj} = \vec{H} - \vec{\sigma}_j$. Substitute it into Equation (2) to construct the analytical

relationship between the wavefront aberration and misalignment values of the misaligned off-axis reflective optical system:

$$W = \sum_j \sum_p^{\infty} \sum_n^{\infty} \sum_m^{\infty} (W_{klm})_j \left[(\vec{H} - \vec{\sigma}_j) \cdot (\vec{H} - \vec{\sigma}_j) \right]^p [(B\vec{\rho} + \vec{d}) \cdot (B\vec{\rho} + \vec{d})]^n \left[(\vec{H} - \vec{\sigma}_j) \cdot (B\vec{\rho} + \vec{d}) \right]^m \quad (3)$$

The ultimate goal of misalignment correction is to optimize the imaging quality of optical systems. For off-axis reflective systems, the degradation of imaging quality caused by component misalignment (specifically manifested as variation in the intensity distribution of the Point Spread Function) is mainly affected by spherical aberration W_{040}, coma W_{131}, and astigmatism W_{222}. Even higher-order aberrations may also be introduced in some complex systems. When only third-order aberrations are taken into account, the aforementioned relational expressions can be expanded as follows:

$$\begin{aligned} W =& B^4 \sum_j (W_{040})_j (\vec{\rho} \cdot \vec{\rho})^2 + B^3 [(\sum_j (W_{131})_j \vec{H}_{Aj} + 4 \sum_j (W_{040})_j \vec{d}) \cdot \vec{\rho}] (\vec{\rho} \cdot \vec{\rho}) \\ &+ B^2 [\frac{1}{2} \sum_j (W_{222})_j \vec{H}_{Aj}^2 + \sum_j (W_{131})_j (\vec{H}_{Aj} \cdot \vec{d}) + 2 \sum_j (W_{040})_j \vec{d}^2] \cdot \vec{\rho}^2 + else \end{aligned} \quad (4)$$

2.2. Analytical Relationship Between Point Spread Function and Misalignment Values Based on Fourier Optics Theory

Based on nodal aberration theory, the mapping relationship between misalignment values and wavefront aberration is established. From the above formula, when there is component misalignment in the off-axis reflective optical system, the wavefront aberration of the pupil plane is a function of FOV, pupil, and misalignment amounts, expressed as:

$$W = W(\vec{H}, \vec{\rho}, \vec{\delta}) \quad (5)$$

where $\vec{\delta}$ represents the vector composed of the misalignment values of each component.

The system wavefront aberration can be accurately characterized by the orthogonal expansion of Fringe Zernike polynomials. Thus, there is a specific relationship between misalignment values and Fringe Zernike polynomial coefficients. According to the nodal aberration theory in Section 2.1, optical system misalignment mainly affects low-order aberrations. Ignoring field curvature, which does not affect imaging sharpness, the wavefront aberration expression is:

$$W(\vec{H}, \vec{\rho}, \vec{\delta}) = \sum_{j=4}^{N} A_j Z_j(\vec{H}, \vec{\rho}, \vec{\delta}) \quad (6)$$

where $Z_j(\vec{H}, \vec{\rho}, \vec{\delta})$ is the Fringe Zernike polynomial. In this paper, j is set to 4 to 9. $j = 4$ corresponds to defocus, $j = 5$ corresponds to 0° astigmatism, $j = 6$ corresponds to 45° astigmatism, $j = 7$ corresponds to X-axis coma, $j = 8$ corresponds to Y-axis coma, and $j = 9$ corresponds to spherical aberration. For some complex systems, j can be set to 4 to 16 or even higher orders according to the actual misalignment correction accuracy requirements. (When the magnitude of changes in Zernike polynomial coefficients above the 9th order caused by position misalignment is non-negligible.) A_j is the sensitivity matrix, reflecting the influence of different misalignment values on aberrations.

To study the influence of aberrations caused by component misalignment on the final imaging of the system, a generalized pupil function is defined as:

$$P(\vec{\rho}, \vec{\delta}) = P_0(\vec{\rho}) \exp\left[ikW(\vec{H}, \vec{\rho}, \vec{\delta})\right] \quad (7)$$

where $k = 2\pi/\lambda$ is the wave number (λ is the working wavelength), and $P_0(\vec{\rho})$ is the ideal aberration-free pupil function, defined as:

$$P_0(x,y) = \begin{cases} 1 & (x,y) \in \text{pupil aperture} \\ 0 & (x,y) \notin \text{pupil aperture} \end{cases} \tag{8}$$

Based on Fourier optics theory, the analytical relationship between the point spread function of the incoherent imaging system and the component misalignment values can be finally obtained:

$$\begin{aligned} I(\vec{H},\vec{\delta}) &= |\mathcal{F}\{P(\vec{\rho})\}|^2 \\ &= \left| \mathcal{F}\left\{ P_0(\vec{\rho}) \exp[jk \sum_{j=4}^{9} A_j Z_j(\vec{H},\vec{\rho},\vec{\delta})] \right\} \right|^2 \end{aligned} \tag{9}$$

where $I(\vec{H},\vec{\delta})$ represents the point spread function of the incoherent imaging system, and $\mathcal{F}\{\cdot\}$ denotes the Fourier transform. When the observed target of the telescope system is a point light source, the PSF of the system is equal to the intensity distribution of the observation result (spot image). This formula indicates that there are clear analytical relationships between the spot image and the misalignment values, as well as between the spot image and the wavefront aberration. In summary, component misalignment will introduce geometric aberrations, which change the Zernike polynomial coefficients and then the wavefront aberration. This is reflected in the PSF as a change in its shape. Therefore, based on Fourier optics, there is a definite mapping relationship between the wavefront aberration changes caused by component misalignment and the PSF changes of the system. This lays a theoretical foundation for the misalignment aberration compensation method for off-axis telescopes fusing spot images and Zernike polynomial coefficients.

3. Misalignment Aberration Compensation Methods Based on Focal Spot Images

3.1. Analysis and Solution of the Multiple-Solution Problem of Focal Spot Images Caused by Misaligned DOFs Coupling

3.1.1. Description of the Multi-Valued Inverse Problem Between Misalignment Values and Focal Spot Images Caused by Aberration Coupling

This paper focuses on the compensation method for low-order aberrations introduced by the deviation of the SM spatial position from the nominal position in an off-axis two-mirror telescope system. As described in Section 2, the aberrations caused by system component misalignment are ultimately reflected in the system's spot images. The high sensitivity of PSF morphology to subtle phase perturbations [30,31] ensures that the aberrations introduced by component misalignment can be fully characterized by the changes in the focal spot image of the off-axis reflective telescope system. A point target at infinity passes through a misaligned telescope system, and its original star-like spot becomes fragmented, as shown in Figure 1. Figure 1a shows the spot image in the ideal state; Figure 1b shows the spot image in the misaligned state. Due to the aberration coupling effect caused by X-axis decenter error (XDE), Y-axis decenter error (YDE), X-axis tilt error (XTE), and Y-axis tilt error (YTE) of the SM, the same PSF morphology may correspond to different misalignment values combinations, as specifically shown in Figures 1c,d. It can be seen from the figures that the two PSFs are basically consistent in morphology, but the true misalignment values are significantly different. This is the multiple-solution problem in the mapping from focal spots to misalignment values. A neural network is essentially a black-box model based on data fitting. The multiple-solution problem will lead to non-convergence of network training and distortion of prediction results. To avoid this problem,

specific constraints need to be imposed on the training dataset to ensure the one-to-one correspondence between focal spot images and misalignment values as much as possible. This ensures that the well-trained neural network does not output false solutions during the misalignment prediction phase.

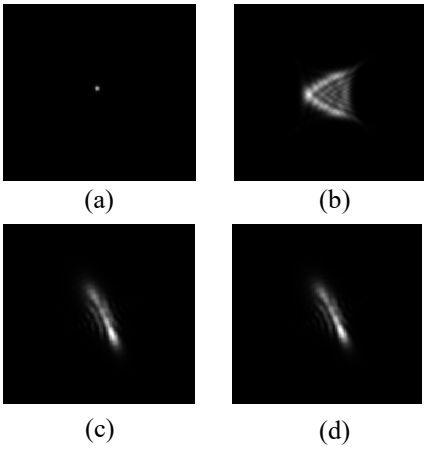


Figure 1. PSF morphology approximation due to misalignments coupling. (**a**) Spot image under nominal state; (**b**) Spot image under misaligned state; (**c**) Misaligned state: $XDE = -0.251$ mm, $YDE = 0.704$ mm, $XTE = 0.486°$, $YTE = -0.299°$; (**d**) Misaligned state: $XDE = -0.331$ mm, $YDE = 0.607$ mm, $XTE = 0.296°$, $YTE = -0.154°$.

Taking the off-axis two-mirror telescope in Section 4 as the research object, to explore the influence of different misaligned DOFs on aberrations, a certain misalignment error is sequentially applied to the four DOFs of the SM (XDE, YTE, YDE, XTE). The variation trends of Fringe Zernike coefficients Z4∼Z9 representing defocus, coma, astigmatism, and spherical aberration are plotted (The order of magnitude of the variation in the coefficients of Z9∼Z16 is much smaller than that of the coefficients of Z4∼Z9). The order and error amounts of adding misalignment errors are $XDE = 1$ mm, $YTE = -2°$, $YDE = 1$ mm, $XTE = 2°$, as shown in Figure 2. Both XDE-YTE and YDE-XTE have severe mutual influences. The aberrations generated can be mutually compensated by applying specific misalignment amount coupling.

To further study the correlation of the influence of different misaligned DOFs on aberrations, the drawn correlation coefficient matrix is shown in Figure 3. The darker the color, the closer the absolute value of the correlation coefficient is to 1, indicating a stronger correlation between variables. The results show that there is a strong positive correlation between X-axis decenter and Y-axis tilt, and a strong negative correlation between Y-axis decenter and X-axis tilt. The aberration generated by X-axis decentration misalignment is basically not affected by the aberrations generated by Y-axis decentration and X-axis tilt misalignment, and the aberration generated by Y-axis decentration misalignment is basically not affected by the aberrations generated by X-axis decentration and Y-axis tilt misalignment. In other words, the multiple-solution problem in the corresponding relationship between the spot shape at the focal point and the misalignment amount is caused by the paired misalignment of two sets of DOF combinations (XDE-YTE and YDE-XTE) with coupled aberrations. Utilizing this characteristic provides empirical guidance for the establishment of the dataset for subsequent neural network training. Selecting almost uncoupled DOFs as all compensation DOFs can avoid the multiple-solution problem as much as possible. This selection also helps improve network training efficiency and solution accuracy. In summary, from the aberration coupling relationship diagram in Figure 2 and the correlation coefficient matrix in Figure 3, two pairs of DOFs can be used

as compensation DOFs, namely the two decenter DOFs (XDE-YDE) and the two tilt DOFs (XTE-YTE).

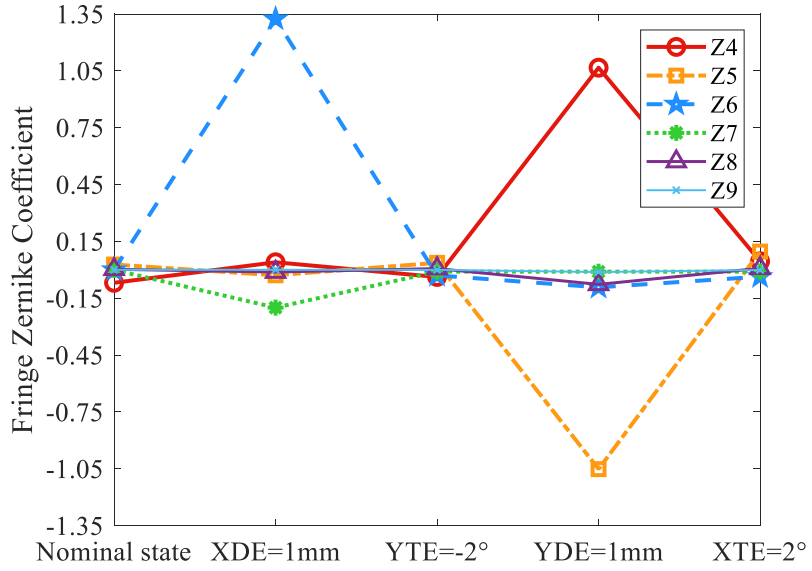


Figure 2. System aberration coupling caused by changes in misalignment values.

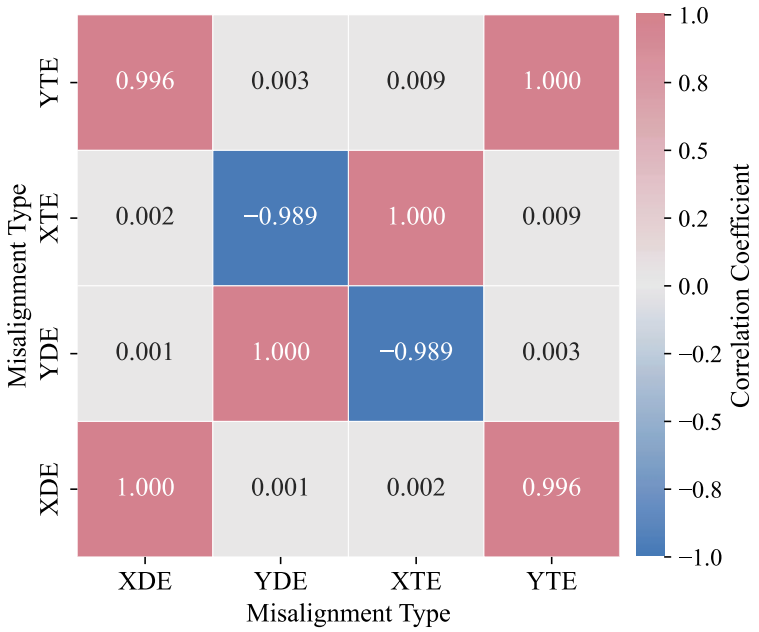


Figure 3. Correlation coefficient matrix of different misaligned DOFs.

3.1.2. Sensitivity Analysis of Misaligned DOFs Based on Mode Truncation Algorithm

Section 3.1.1 has determined the DOF combinations that can be used for aberration compensation. According to the principle of completing misalignment-induced aberration correction with the minimum compensation amount input, it is necessary to determine the specific compensation strategy through sensitivity analysis of misaligned DOFs. Sensitivity reflects the influence of unit misalignment value of misaligned DOFs on aberrations. This paper employs an SVD-based mode truncation algorithm to conduct sensitivity analysis on misaligned DOFs. By decomposing the sensitivity matrix reflecting the sensitivity relationship between wavefront aberration and misalignment values, the DOF combination with the highest aberration compensation sensitivity is selected. Taking the off-axis two-mirror telescope in Section 4 as an example, after selecting FOV points, data for the

sensitivity matrix are collected. A large number of random disturbance misalignment values within the range of ±2 mm and ±2° are independently applied to the four lateral misalignment DOFs of the SM, and Fringe Zernike terms Z4∼Z9 of multiple FOVs are collected. Linear fitting is performed on the data. The first-order coefficient of the fitted function is the element of the sensitivity matrix, which is arranged according to rules to form the sensitivity matrix A. According to the classic SVD method, the sensitivity matrix A can be expressed as:

$$A = U\Sigma V^T \tag{10}$$

where U and V are the left and right singular matrices, respectively, Σ is the diagonal matrix whose main diagonal elements are the eigenvalues of A. The mode truncation algorithm based on SVD is an iterative algorithm. In each iteration, the least sensitive variable among the selected compensation variables is truncated and eliminated from the sensitivity matrix A. Figure 4 shows the sensitivity analysis flow of the SVD-based mode truncation algorithm. The iteration ends after reaching the artificially set number of times k, where k represents the k least sensitive items among all disturbance factors. The DOFs corresponding to the columns eliminated from them are the currently least sensitive DOFs, thereby completing the sensitivity ranking.

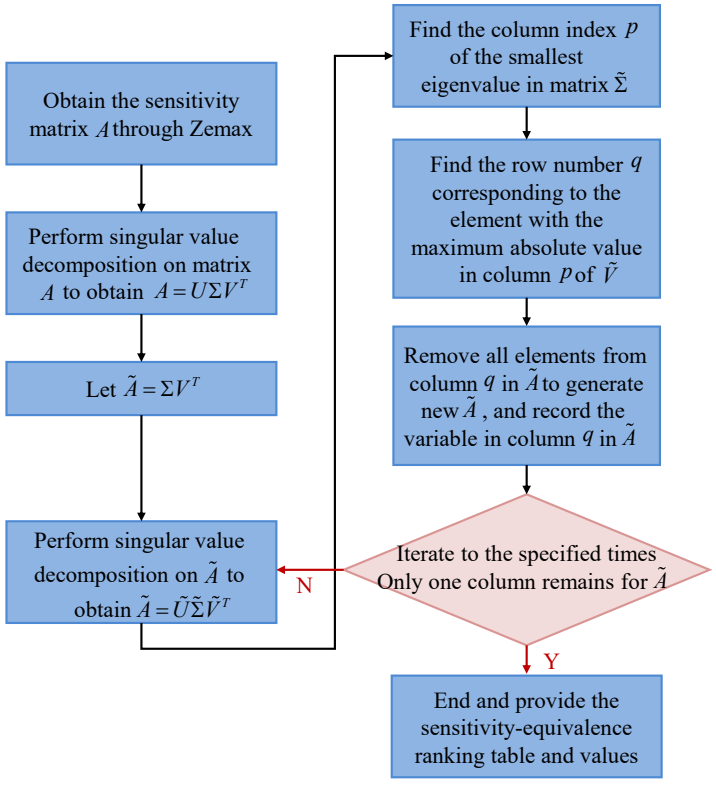


Figure 4. Sensitivity analysis flow using SVD-based mode truncation algorithm.

Taking the off-axis two-mirror telescope in Section 4 as an example, the mode truncation algorithm completes the sensitivity ranking of the four misaligned DOFs relative to aberrations after 4 iterations. The operational sensitivity ranking is obtained after unifying the units, and the results are shown in Table 1.

Table 1. Sensitivity ranking of misaligned DOFs.

DOF	Sensitivity	Sensitivity Unit	Operational Sensitivity
YDE	3.6167	mm^{-1}	14.4668
XDE	2.9942	mm^{-1}	11.9776
YTE	0.0703	deg^{-1}	0.2812
XTE	0.0696	deg^{-1}	0.2792

It can be seen from Table 1 that after unifying the units, the X-axis and Y-axis decenter operational DOFs are higher. Moreover, as known from Section 3.1.1, the coupling is also small. Considering comprehensively, the two DOFs of X-axis and Y-axis decenter are used to compensate for the misalignment of the four DOFs of X-axis/Y-axis decenter and tilt. This provides guidance for the establishment of the dataset for subsequent neural network model training.

3.2. Misalignment-Induced Aberration Compensation Method for Off-Axis Telescopes Fusing Spot Images and Zernike Coefficients

According to the NAT and Fourier optics theory in Section 2, it is proved that there are specific analytical relationships between the system's spot images, Zernike polynomial coefficients, and component misalignment values. Based on this, this paper proposes two novel misalignment aberration compensation methods for off-axis telescopes based on focal spot images. The first method constructs a mathematical model between focal spot images and misalignment amounts directly based on a CNN model. On this basis, utilizing the characteristic that Zernike polynomials can effectively characterize system aberrations, an improved misalignment aberration compensation method fusing focal spot images and Zernike coefficients is proposed. The algorithm flow chart is shown in Figure 5. The mapping relationship between spot images and Zernike coefficients is established based on a CNN model, and the nonlinear relationship between Zernike coefficients and misalignment amounts is fitted based on a FCNN model. After the two network models are trained, the weights are combined to form a new weight model. In the actual aberration correction process, both methods do not require aberration detection. Only a single focal spot image needs to be collected and input into the trained network model to solve for the misalignment compensation amount in one step. This method has low hardware requirements and relatively fixed network parameters, making it easy for relevant technical personnel to operate.

The schematic diagram of model training based on MobileNetV3-Small and FCNN is shown in Figure 6. The specific implementation steps of the misalignment-induced aberration compensation method for off-axis telescopes fusing spot images and Zernike coefficients are as follows. Taking an off-axis two-mirror telescope as an example, it is divided into neural network training and actual misalignment correction processes:

(1) Construct a dataset for neural network model training of the system to be misaligned and corrected. Specific steps: Build an off-axis reflective telescope system. Record the ideal spatial position of the SM relative to the primary mirror when the system is fully aligned, as well as the spot image and the wavefront PV and RMS values of each FOV in this state. According to the analysis in Section 3.1, to ensure that the neural network model learns the unique mapping between spot images and misalignment, it is necessary to select two almost uncoupled misaligned DOFs to construct the training set. Add known uncoupled two-DOF misalignment values to the SM. Use a CCD camera to collect the PSF in this state and a wavefront detector such as an interferometer to obtain Zernike polynomial coefficients representing system aberrations. Take the PSF and Zernike polynomial coefficients as one set of samples, and the Zernike polynomial coefficients and

misalignment amounts as another set of samples. Repeat the above steps multiple times to form a complete dataset.

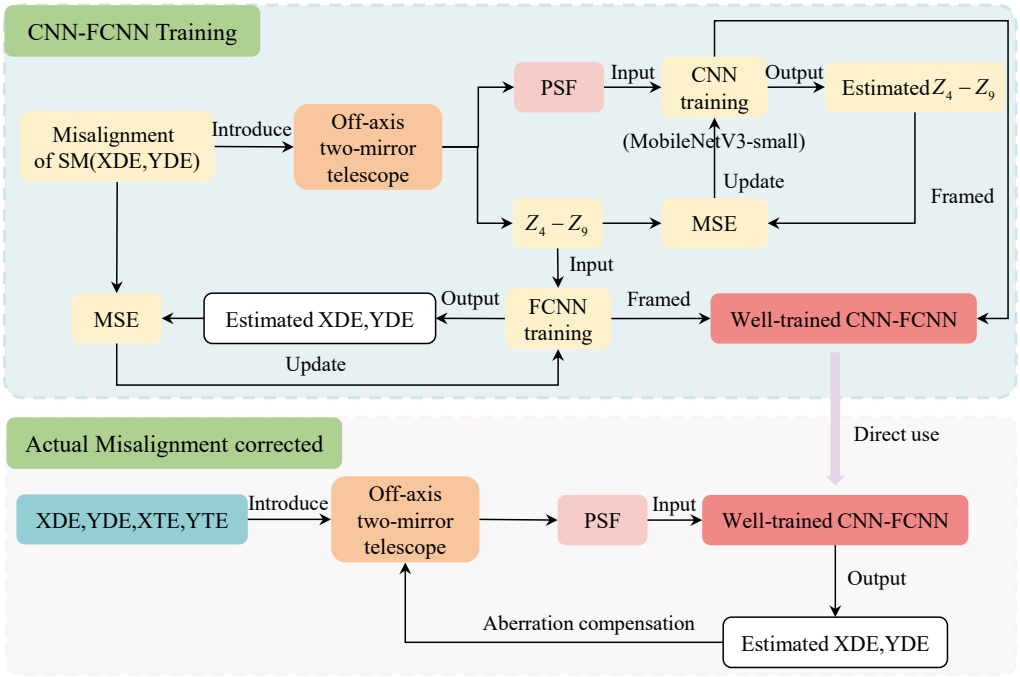


Figure 5. Flow chart of the misalignment-induced aberration compensation method based on fusion of focal spot images and Zernike polynomial coefficients.

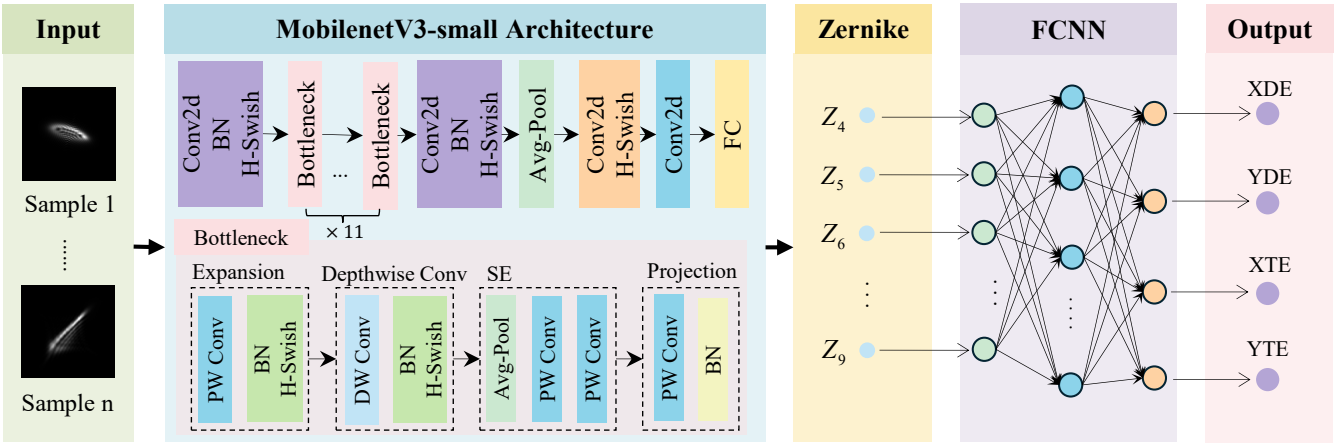


Figure 6. Schematic diagram of model training based on MobileNetV3-Small and FCNN.

(2) Select appropriate network model structures and parameters for the two parts of the network. Train the neural network models using the training set. After the two network models are trained, combine their weights to form a new weight model, thereby establishing the mapping relationship between focal spot images and misalignment values.

(3) In the actual misalignment correction process of the telescope system. No wavefront detector is required to acquire the coefficients of Zernike polynomials. First, use a CCD camera to collect a single focal spot image of the system. Input it into the combined neural network model. Then output the SM misalignment compensation amount. Input it into the six-DOF platform of the actuator that controls the SM spatial position to guide the alignment of the primary and secondary mirrors. Collect the system's spot image again for image quality evaluation. If the image quality meets the requirements, the alignment

process of the primary and secondary mirrors is completed. Otherwise, repeat the above steps to form closed-loop control.

4. Verification

In this section, the feasibility of the proposed method is verified through a detailed misalignment correction simulation process of the off-axis two-mirror telescope. The superiority of the proposed misalignment aberration compensation method for off-axis telescopes based on fusion of spot images and Zernike coefficients is verified from both misalignment value solution accuracy and wavefront aberration correction performance.

In this paper, a lightweight neural network MobileNetV3-Small [32] is selected to establish the mathematical model between spot images and Zernike polynomial coefficients. The network structure is shown in Figure 5, and the training parameters are shown in Table 2. MobileNetV3-Small is selected for mapping spot images to Zernike polynomial coefficients due to its excellent compatibility with research requirements. Firstly, its lightweight design (adopting a lightweight channel attention mechanism and depthwise separable convolutions) significantly reduces computational complexity and parameter count, enabling efficient operation on telescope embedded systems with limited hardware resources and meeting real-time misalignment correction needs. Secondly, the integrated squeeze-and-excitation (SE) module and H-Swish activation function enhance the network's ability to extract subtle intensity distribution features of spot images, which is crucial for capturing aberration-related information encoded in Zernike coefficients. Thirdly, it achieves a balanced performance between feature extraction depth and overfitting resistance, which is well-suited for the constructed dataset scale (5000 groups of samples), avoiding the inefficiency of overly deep networks or insufficient feature extraction of shallow networks. Its proven generalization in image feature extraction tasks further ensures reliable performance in the specific scenario of spot image and Zernike coefficient mapping. Therefore, MobileNetV3-Small can achieve favorable misalignment solution performance at a relatively low computational cost. Considering the nonlinear relationship between Zernike polynomial coefficients and misalignment amounts and that both are numerical data, a fully connected neural network suitable for regression problems is selected to fit the mapping relationship between Zernike polynomial coefficients and misalignment values. The network training parameters are set as shown in Table 3. Minor adjustments are made according to changes in input and output parameters of different experiments.

Table 2. Network training parameters based on MobileNetV3.

Batch Size	Initial Learning Rate	Loss Function	Epoch	Optimizer
16	0.0001	MSE	1000	AdamW

Table 3. Network training parameters based on the FCNN.

Input Number	Output Number	Number of Layers	Number of Hidden Layer Neurons	Dropout Rate
30	4	5	50∼500	0.5
Batch Size	**Initial Learning Rate**	**Loss Function**	**Epoch**	-
256	0.01	MSE	10,000	-

The 3D layout of the off-axis two-mirror telescope model used in the experiments of this section is shown in Figure 7, and the optical parameters of each surface are listed in Table 4. Its effective focal length is 1237.63 mm, the system's F-number is 12.4148, the entrance pupil diameter is 100 mm, the pupil off-axis amount is 100 mm, and the working wavelength is 10 μm. Under the ideal nominal state of the model, the wavefront PV value of the central 0° field of view (FOV1) is 0.2146λ, the RMS value is 0.0478λ; the wavefront PV value of the 0.27° field of view (FOV2) is 0.4005λ, the RMS value is 0.0827λ; the wavefront PV value of the 0.386° field of view (FOV3) is 0.4529λ, the RMS value is 0.0935λ.

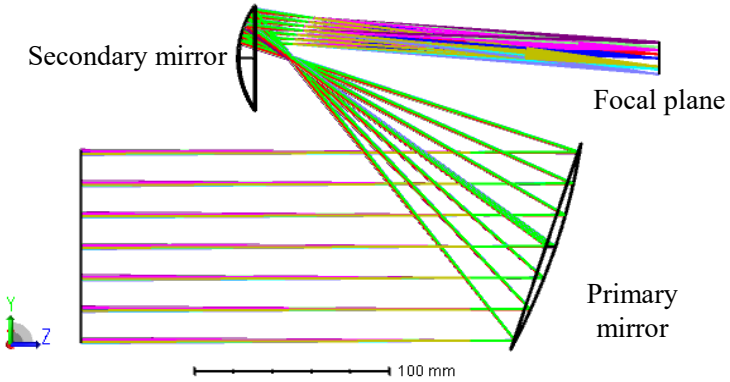


Figure 7. The optical layout of the off-axis two-mirror telescope system.

Table 4. Optical mirror parameters of the off-axis two-mirror telescope system.

Surface	Diameter/mm	Thickness/mm	Radius of Curvature/mm	Conic Factor
Primary mirror	110	−178.590	−304.260	−1.009
Secondary mirror	56	26.702	47.127	−0.568

4.1. Misalignment Value Solution Accuracy Test

To intuitively verify the training effect of the neural network model, the labels of the test set and training set only include the misalignment amounts of the two compensation DOFs of X/Y-axis decenter. Two misalignment error ranges are set: a large misalignment range where both XDE and YDE are (−2, +2) mm, and a medium misalignment range of (−1, +1) mm. A total of 5000 groups of misalignment samples involving X-axis and Y-axis decenter are generated, among which 4000 groups are randomly selected as the training set and 1000 groups as the validation set. The model with the minimum validation set loss is saved during the network training process. Several new test sets with random misalignment within a certain range is then regenerated to verify the nonlinear fitting capability of the neural network. The focal spot images for testing are input into the trained neural network model to solve the corresponding misalignment amounts, which are then compared with the true values. Mean absolute error (MAE) and root mean square error (RMSE) are used as evaluation indicators. MAE can effectively avoid mutual cancellation of errors and truly reflect the absolute deviation level of a single solution. RMSE can highlight the impact of large deviations on overall accuracy and more comprehensively characterize the solution stability of the model. First, to determine the optimal training sample size, a comparative experiment on the solution accuracy of misalignment amounts with different sample sizes (2000, 5000 and 10,000 groups) is designed based on the MobileNetV3-Small architecture, with the MAE of X-axis decenter (XDE) and Y-axis decenter (YDE) as the evaluation index. The experimental results are presented in Table 5. It can be seen from Table 4 that when the sample size is increased to 10,000 groups, although the accuracy

is continuously improved, the data acquisition costs (including the time consumed by simulation experiments and hardware resource occupation) and model training time increase exponentially. Combined with the misalignment correction objective of this study (the wavefront RMS residual after correction is close to the nominal state and less than 0.003λ), 5000 groups of samples can fully meet the accuracy requirements of the research and achieve a balance between accuracy and cost. In subsequent practical applications, the sample size can be flexibly selected according to specific scenarios. Subsequently, a comparative experiment is conducted to evaluate the solution accuracy of misalignment amounts of the two methods under different misalignment ranges. It can be seen from Table 6 that whether in the large misalignment range of (−2, +2) mm or the medium misalignment range of (−1, +1) mm, the solution accuracy of the CNN-FCNN fusion model is significantly better than that of the CNN model. In the range of (−2, +2) mm, the overall error of XDE and YDE solution by the CNN-FCNN model is reduced by more than 30% compared with the CNN model. In the medium misalignment range of (−1, +1) mm, the solution accuracy of both models is improved, and the advantage of the CNN-FCNN model is more significant, with an error reduction of more than 35%. This indicates that the CNN-FCNN fusion model has higher solution accuracy in different misalignment amount scenarios.

Table 5. Misalignment solution accuracy under different sample sizes based on MobileNetV3-Small.

Sample Size	XDE	YDE
2000	0.0068	0.0055
5000	0.0060	0.0041
10,000	0.0030	0.0024

Table 6. The MAE and RMSE of misalignment solution.

Method	(−2, 2) mm				(−1, 1) mm			
	XDE		YDE		XDE		YDE	
	MAE	RMSE	MAE	RMSE	MAE	RMSE	MAE	RMSE
CNN	0.0120	0.0145	0.0100	0.0130	0.0060	0.0075	0.0041	0.0051
CNN-FCNN	0.0076	0.0096	0.0085	0.0112	0.0039	0.0049	0.0029	0.0036

From the scatter distribution characteristics in Figure 8, all test sample points are closely clustered near the ideal fitting line ($y = x$, where the abscissa represents the actual misalignment value and the ordinate represents the estimated misalignment value) without obvious deviation trend. This intuitively proves that the mapping relationship between spot images and misalignment amounts established by the CNN-FCNN fusion model has good linear consistency and stability. To further analyze the absolute error distribution characteristics of misalignment value solution for all test samples, Figure 9 shows a comparison of the absolute error ratio distribution of the two models within the misalignment range of (−1, +1) mm. For XDE solution, 95.2% of the samples of the CNN-FCNN model have an error not exceeding 0.01 mm; while the proportion of samples with an error exceeding 0.01 mm in the CNN model reaches 17.8%. For YDE solution, the proportion of samples with an error of 0∼0.007 mm in the CNN-FCNN model reaches 94.7%, which is much higher than that of the CNN model. The above data fully indicates that the CNN-FCNN fusion model effectively extracts the core information related to misalignment amounts from spot images by introducing Zernike coefficients as an intermediate feature bridge. It greatly reduces the solution error and lays a preliminary

model training foundation for subsequent proof of the superiority of using two-DOF compensation for four-DOF.

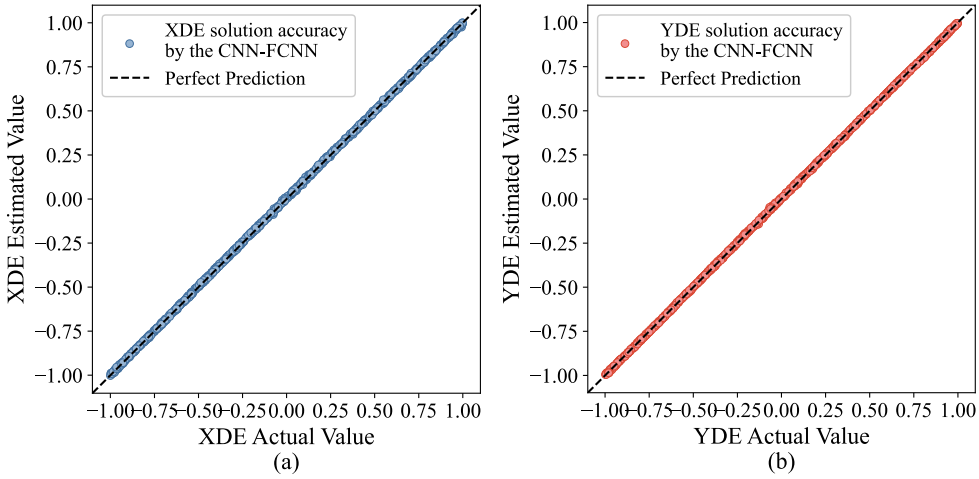


Figure 8. Comparison between estimated and actual misalignment value obtained by CNN-FCNN (abscissa: actual misalignment value, ordinate: estimated misalignment value, dashed line represents ideal fitting line $y = x$). (**a**) Scatter plot of X-axis decenter error solution accuracy; (**b**) Scatter plot of Y-axis decenter error solution accuracy.

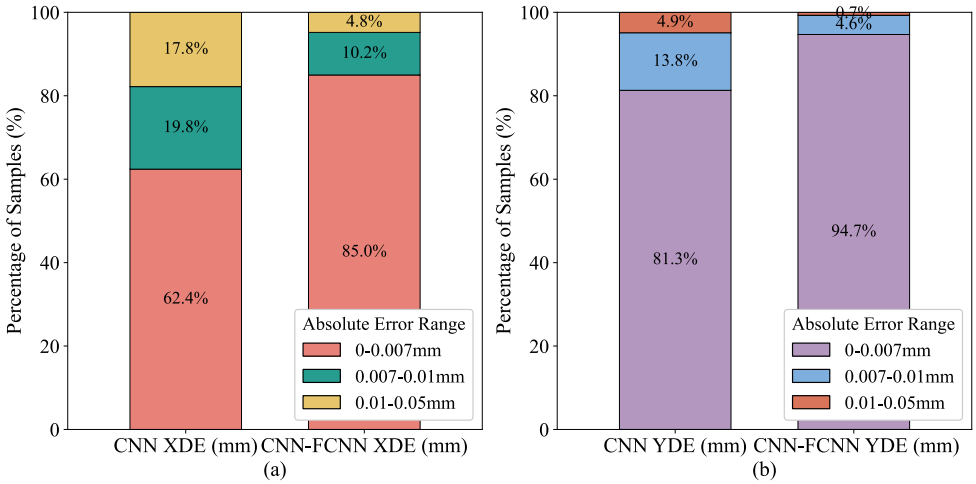


Figure 9. Comparison of absolute error ratio distributions of misalignment solutions by two methods. (**a**) Comparison of absolute error percentages of X-axis decenter error solution based on CNN and CNN-FCNN. (**b**) Comparison of absolute error percentages of Y-axis decenter error solution based on CNN and CNN-FCNN.

4.2. Wavefront Aberration Correction Performance Demonstration

In practical engineering scenarios, after correcting the axial misalignment of the secondary mirror, the lateral misalignment of the off-axis telescope often manifests as coupled misalignment of four DOFs: XDE, YDE, XTE, and YTE. At this time, it is difficult to directly compare the accuracy of the two-DOF compensation solution with the four-DOF actual values. Therefore, this section quantifies and verifies the correction effect of the method by evaluating the wavefront aberration indicators (PV value, RMS value) of the system after correction. The wavefront PV and RMS values of each FOV after correction are compared with those of the nominal design state and the uncorrected misaligned state. The experiment selects 3 FOVs of the system (FOV1: 0° central FOV, FOV2: 0.27° FOV, FOV3: 0.386° FOV). Artificial four-DOF coupled misalignment is set: the XDE and YDE decenter error ranges are ±0.6 mm, and the XTE and YTE tilt error ranges are ±0.4°. Collect

the focal spot images under this misaligned state and input them into the trained model. Obtain the compensation solution and apply it to the SM adjustment mechanism. Record the wavefront information of the three FOVs after correction. Compare them with the three FOVs in the nominal state. Calculate the MAE of the PV and RMS residuals of each FOV to characterize the stability of the correction performance.

Table 7 shows that the misalignment correction effect of the CNN model is significantly better than that of the traditional sensitivity matrix method (SM). The correction effect of the CNN-FCNN fusion model is further improved. Compared with the CNN model, the average MAE of residuals is reduced by more than 25%, especially the correction effect in the central FOV is the most prominent, which is closer to the ideal design state.

Table 7. MAE of wavefront aberration PV and RMS residuals.

Method	FOV1(λ)		FOV2(λ)		FOV3(λ)	
	PV	RMS	PV	RMS	PV	RMS
SM	0.0559	0.0122	0.0586	0.0129	0.0595	0.0128
CNN	0.0178	0.0036	0.0157	0.0036	0.0163	0.0039
CNN-FCNN	0.0099	0.0024	0.0133	0.0029	0.0147	0.0034

Figure 10 shows an intuitive comparison of the average wavefront PV and RMS values of each FOV after misalignment correction of all test samples using three methods. Taking the central 0° FOV (FOV1) as an example, the wavefront PV value and RMS value after misalignment correction using the sensitivity matrix method are significantly higher than those in the nominal design state (the wavefront PV value is 0.2146λ and the RMS value is 0.0478λ in the nominal design state). After compensating for the aberrations caused by four-DOF misalignment using the CNN model, the wavefront PV value and RMS value are reduced but still higher than those in the nominal design state. After misalignment compensation using the CNN-FCNN model, the wavefront is closest to the nominal design state. In summary, the misalignment aberration compensation method fusing spot images and Zernike coefficients is the most superior.

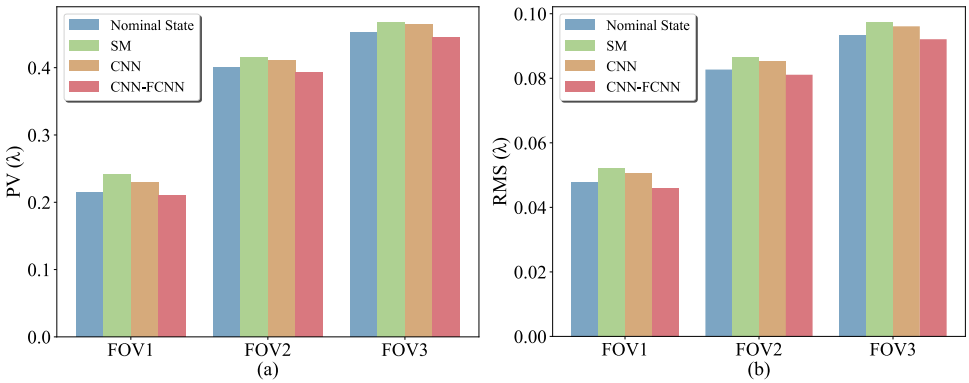


Figure 10. Comparison of wavefront correction effects by three methods. (**a**) Comparison of wavefront aberration PV values of three FOVs under SM, CNN, CNN-FCNN misalignment correction and nominal design states (**b**) Comparison of wavefront aberration RMS values of three FOVs under SM, CNN, CNN-FCNN misalignment correction and nominal design states.

The scatter plots of wavefront aberrations of 500 groups of test samples in Figure 11 further reveal the changes in aberration distribution before and after correction based on the CNN-FCNN model. Before correction (green dots, purple dots), the PV and RMS values of each FOV are widely scattered and the overall values are relatively high; after correction (red dots, blue dots), all sample points are clustered near the ideal values, and the dispersion

degree is significantly reduced. This indicates that the correction effect of the CNN-FCNN model has good consistency and stability, and can effectively suppress the image quality degradation caused by different degrees of coupled misalignment. Figure 12 randomly selects a group of samples to compare the wavefront parameters and spot morphology, intuitively showing the misalignment correction effect. Under the misaligned state, the spot is speckled, the PV value exceeds 2.2λ, and the RMS value exceeds 0.37λ. After correction by the CNN-FCNN model, the spot is restored to a regular circular spot, and the PV and RMS values of each FOV are close to the ideal state. Among them, the PV value of FOV1 is 0.2172λ, and the RMS value is 0.0483λ, the difference from the ideal value is negligible.

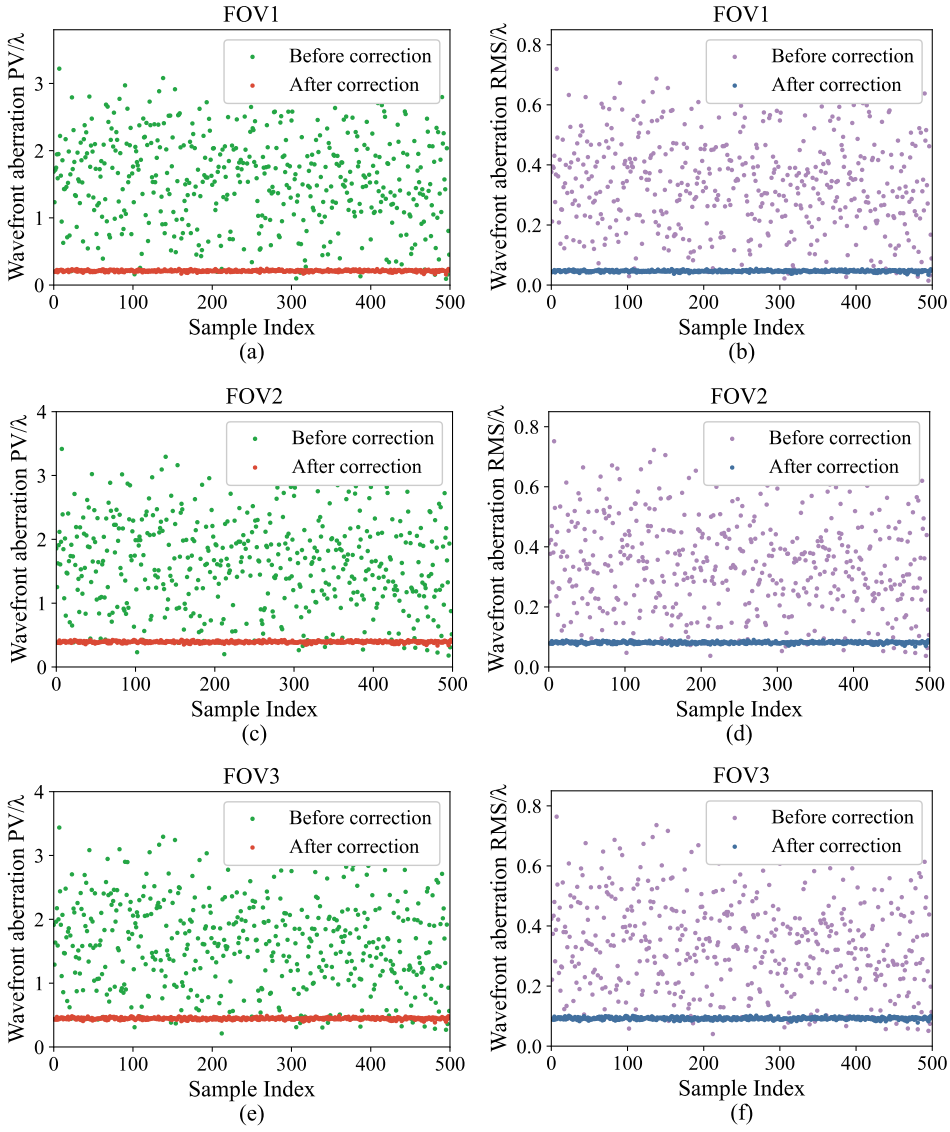


Figure 11. Scatter plots of wavefront aberrations before and after correction based on CNN-FCNN. (**a**,**c**,**e**) respectively represent the comparison of wavefront aberration PV of 500 groups of samples in three FOVs before and after correction. Green dots represent the distribution of wavefront aberration PV before correction, and red dots represent the distribution of wavefront aberration PV after correction. (**b**,**d**,**f**) respectively represent the comparison of wavefront aberration RMS of 500 groups of samples in three FOVs before and after correction. Purple dots represent the distribution of wavefront aberration RMS before correction, and blue dots represent the distribution of wavefront aberration RMS after correction. .

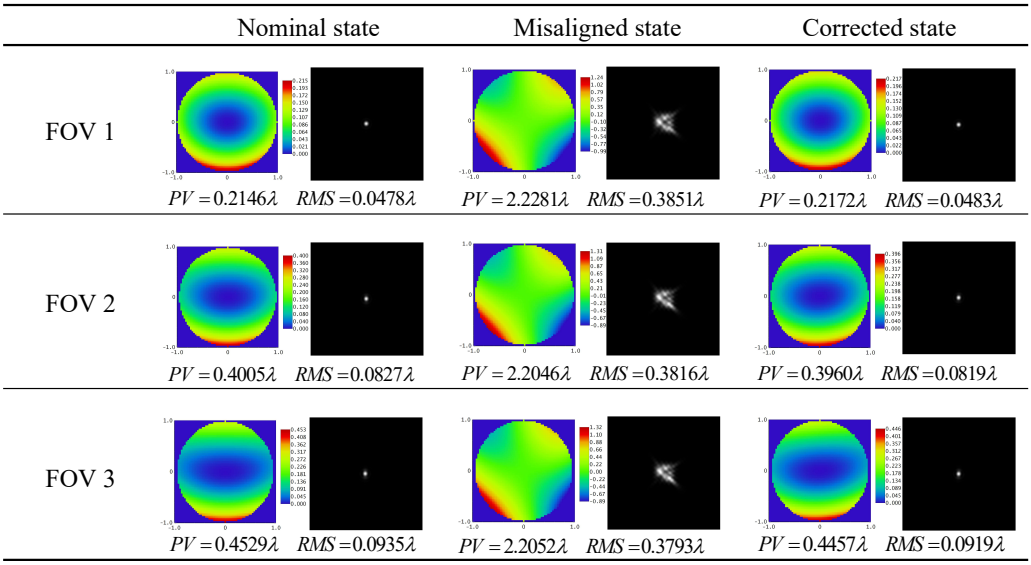


Figure 12. Misalignment correction effect.

In practical application scenarios, detector noise can affect the quality of collected spot images, thereby reducing misalignment correction accuracy. To further discuss the robustness of the proposed method, different levels of noise (evaluated by peak signal-to-noise ratio, PSNR) are added to the test spot images. The root mean square deviation (RMSE) between the wavefront RMS of the corrected state and the nominal state before misalignment correction is calculated. The relationship between the misalignment correction accuracy of the proposed CNN-FCNN method and the noise level is shown in Figure 13. The results indicate that the alignment accuracy of the method is actually related to the noise level. As the peak signal-to-noise ratio increases, the system's alignment accuracy gradually improves. When the peak signal-to-noise ratio is greater than 30 dB, the misalignment correction accuracy is close to the noise-free state. However, when the PSNR is less than 30 dB, the algorithm's correction accuracy is relatively low. In future work, the influence of various types of noise should be considered to further improve the robustness of the algorithm.

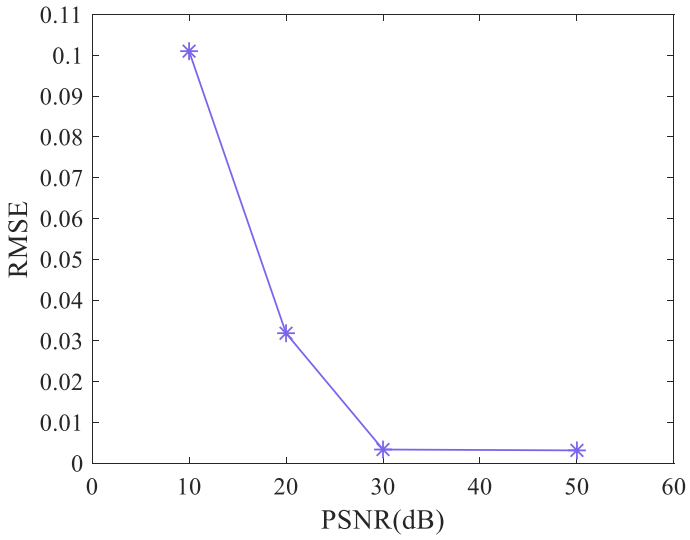


Figure 13. The relationship between the misalignment correction accuracy of the proposed CNN-FCNN method and the noise level.

In summary, both from the quantitative index level of wavefront aberration residuals and the intuitive characterization level of spot morphology, the misalignment aberration compensation method fusing focal spot images and Zernike coefficients proposed in this paper exhibits excellent correction performance. Its accuracy is significantly better than that of the CNN model and the sensitivity matrix method, which can effectively solve the correction problem of four-DOF coupled misalignment of off-axis telescopes and ensure that the system imaging quality approaches the ideal design state.

5. Conclusions

Taking an off-axis two-mirror system as an example, this study proposes two methods for directly solving SM misalignment compensation amounts through a single focal spot image. First, based on vector wavefront aberration theory and Fourier optics, the analytical relationships between the system's PSF, Zernike polynomial coefficients, and misalignment amounts are established to lay a theoretical foundation. Then, considering that different misalignment amount combinations correspond to similar focal spot images, to ensure the accuracy of neural network learning, an SVD-based mode truncation algorithm is used to conduct sensitivity analysis of different misalignment DOFs and propose an aberration compensation strategy to avoid this problem. This study proposes to directly establish the mapping relationship between focal spot images and misalignment amounts based on a CNN. On this basis, it further proposes to establish the mapping relationship between spot images and Zernike polynomial coefficients based on a CNN, and fit the nonlinear relationship between Zernike polynomial coefficients and misalignment amounts based on a FCNN model. After the two network models are trained, they are combined to form a new weight model for the new misalignment aberration compensation algorithm.

In the actual aberration correction process, both methods do not require aberration detection. Only a single focal spot image needs to be collected and input into the trained network model to solve for the misalignment compensation amount in one step. Input it into the displacement control platform to realize the misalignment correction of the off-axis telescope. Simulation results show that when only the focal spot image of the central FOV is collected, after aberration compensation using the two proposed methods, the wavefront aberration PV and RMS values of the central FOV and two edge FOVs are close to the nominal design state. The focal spot image is restored from a speckled state to a circular spot state. From the comparative experiments, it can be seen that adding a process of extracting Zernike polynomial coefficient features from spot images can more effectively establish the connection between spot images and misalignment amounts, and achieve better misalignment aberration compensation effect. Both methods are significantly better than the traditional sensitivity matrix method based on wavefront aberration detection in the large misalignment range. The misalignment aberration compensation method for off-axis reflective telescopes proposed in this study does not depend on the accuracy of wavefront detection and does not require multiple iterations. It balances accuracy and efficiency and ensures the final imaging quality of the system. However, this algorithm also has certain limitations and is mainly applicable to focused telescope systems with perfectly coupled lateral misalignment DOFs. To ensure the misalignment correction effect of telescopes with different parameters, in the actual application of this algorithm, it is necessary to perform separate data collection (including as large a misalignment range as possible to cope with most scenarios) and model training for each specific optical system.

Author Contributions: Conceptualization, W.T. (Wei Tang) and Y.H.; Methodology, Y.L. and W.T. (Wei Tang); Software, W.T. (Weihua Tang), J.F. and S.T.; Validation, W.T. (Wei Tang), Y.L., and W.T. (Weihua Tang); Formal Analysis, W.T. (Wei Tang) and Y.L.; Investigation, J.F. and S.T.; Resources, Y.H.; Data Curation, W.T. (Wei Tang) and Y.L.; Writing—Original Draft Preparation, W.T. (Wei Tang) and Y.L.; Writing—Review & Editing, W.T. (Wei Tang), Y.L., and Y.H.; Visualization, W.T. (Wei Tang) and J.F.; Supervision, Y.H.; Project Administration, Y.H. All authors have read and agreed to the published version of the manuscript.

Funding: This research received no external funding.

Data Availability Statement: Data underlying the results presented in this paper are not publicly available at this time based on data protection policy but may be obtained from the authors via email upon reasonable request.

Conflicts of Interest: The authors declare no conflicts of interest. The funders had no role in the design of the study; in the collection, analyses, or interpretation of data; in the writing of the manuscript; or in the decision to publish the results.

References

1. Fischer, R.E.; Tadic-Galeb, B. *Optical Systems Design*; McGraw-Hill: New York, NY, USA, 2000.
2. Hopkins, H.; Tiziani, H.J. A theoretical and experimental study of lens centering errors and their influence on optical image quality. *Br. J. Appl. Phys.* **1966**, *17*, 33–55. [CrossRef]
3. Gu, Z.; Yan, C.; Wang, Y. Alignment of a three-mirror anastigmatic telescope using nodal aberration theory. *Opt. Express* **2015**, *23*, 25182–25201. [CrossRef]
4. Zhang, X.; Zhang, D.; Xu, S.; Ma, H. Active optical alignment of off-axis telescopes based on nodal aberration theory. *Opt. Express* **2016**, *24*, 26392–26413. [CrossRef]
5. Zhang, X.; Xu, S.; Ma, H.; Yan, C. Optical compensation for the perturbed three-mirror anastigmatic telescope based on nodal aberration theory. *Opt. Express* **2017**, *25*, 12867–12883. [CrossRef]
6. Wen, M.; Han, C.; Ma, H. Active compensation for optimal RMS wavefront error in perturbed off-axis optical telescopes using nodal aberration theory. *Appl. Opt.* **2021**, *60*, 1790–1800. [CrossRef]
7. Bai, X.; Ju, G.; Ma, H.; Yan, C. Aberrational interactions between axial and lateral misalignments in pupil-offset off-axis two-mirror astronomical telescopes. *Appl. Opt.* **2019**, *58*, 7693–7707. [CrossRef]
8. Bai, X.; Xu, B.; Ju, G.; Ma, H. Aberration compensation strategy for the radius of curvature error of the primary mirror in off-axis three-mirror anastigmatic telescopes. *Appl. Opt.* **2021**, *60*, 6199–6212. [CrossRef]
9. Figoski, J.W.; Shrode, T.E.; Moore, G.F. Computer-aided alignment of a wide-field, three-mirror, unobscured, high-resolution sensor. *Proc. SPIE* **1989**, *1049*, 166–177.
10. Kim, S.; Yang, H.S.; Lee, Y.W.; Kim, D. Merit function regression method for efficient alignment control of two-mirror optical systems. *Opt. Express* **2007**, *15*, 5059–5068. [CrossRef] [PubMed]
11. Lee, H.; Dalton, G.B.; Tosh, I.A.J.; Kim, S.-W. Computer-guided alignment II: Optical system alignment using differential wavefront sampling. *Opt. Express* **2007**, *15*, 15424–15437. [CrossRef] [PubMed]
12. Oteo, E.; Arasa, J. New strategy for misalignment calculation in optical systems using artificial neural networks. *Opt. Eng.* **2013**, *52*, 074105. [CrossRef]
13. Liu, Z.; Peng, Q.; Xu, Y.; Ren, G.; Ma, H. Misalignment calculation on off-axis telescope system via fully connected neural network. *IEEE Photonics J.* **2020**, *12*, 0600112. [CrossRef]
14. Platt, B.C.; Shack, R. History and principles of Shack-Hartmann wavefront sensing. *J. Refract. Surg.* 2001, 17, S573–S577. [CrossRef]
15. Roddier, F. Curvature sensing and compensation: A new concept in adaptive optics. *Appl. Opt.* **1988**, *27*, 1223–1225. [CrossRef] [PubMed]
16. Tsukui, R.; Kino, M.; Yamamoto, K.; Ohta, J. Point-diffraction interferometer wavefront sensor with birefringent crystal. *Appl. Opt.* **2020**, *59*, 8370–8379. [CrossRef]
17. He, Y.; Bao, M.; Chen, Y.; Ye, H.; Fan, J.; Shi, G. Accuracy characterization of Shack–Hartmann sensor with residual error removal in spherical wavefront calibration. *Light. Adv. Manuf.* **2023**, *4*, 393–403. [CrossRef]
18. Khorin, P.A.; Dzyuba, A.P.; Khonina, S.N. Optical wavefront aberration: Detection, recognition, and compensation techniques–a comprehensive review. *Opt. Laser Technol.* **2025**, *191*, 113342. [CrossRef]
19. Zhou, G.; Liu, Z.; Zhou, X.; Zhang, H.; Xu, C.; Zhao, D.; Lin, J.; Wu, G. Internal Stray Light Suppression for Single-Band Bathymetric LiDAR Optical System. *IEEE Trans. Instrum. Meas.* **2024**, *73*, 7007112. [CrossRef]

20. Zhou, G.; Song, N.; Jia, G.; Wu, J.; Gao, K.; Huang, J. Adaptive adjustment for laser energy and PMT gain through self-feedback of echo data in bathymetric LiDAR. *IEEE Trans. Geosci. Remote Sens.* **2024**, *62*, 4206422. [CrossRef]
21. Jiang, W.; Liu, L.; Bu, Y. Application of deep learning in the phase processing of digital holographic microscopy. *Photonics* **2025**, *12*, 810. [CrossRef]
22. Li, M.; Liu, C.; Zhang, J. Multi-stage learning strategies for phase unwrapping under severe speckle noise. *Opt. Express* **2024**, *32*, 16890–16905. [CrossRef]
23. Li, M.; Liu, X.; Zhang, A.; Ma, H. Telescopes alignment using the sharpness function method based on undersampled images. *IEEE Photonics J.* **2019**, *11*, 6800814. [CrossRef]
24. Bai, X. Active alignment of space astronomical telescopes by matching arbitrary multi-field stellar image features. *Opt. Express* **2021**, *29*, 23542–23558. [CrossRef]
25. Jia, P.; Li, X.Y.; Li, Z.Y.; Liu, C.; Ma, H. Point spread function modelling for wide field small aperture telescopes with a denoising autoencoder. *Mon. Not. R. Astron. Soc.* **2020**, *480*, 2466–2474. [CrossRef]
26. Gu, Y.; Zhang, X.F.; Li, B.D.; Ma, H. Deep-learning for position error detection of the secondary mirror in space optical remote sensing system. In *Proceedings of the 7th Asia Pacific Conference on Optics Manufacture and 2021 International Forum of Young Scientists on Advanced Optical Manufacturing (APCOM and YSAOM 2021)*; SPIE: Wales, UK, 2022.
27. Li, B.D.; Zhang, X.F.; Gu, Y.; Ma, H. Active compensation for perturbed coaxial reflecting space telescope using defocus point spread function and convolutional neural network. *Opt. Commun.* **2023**, *537*, 129451. [CrossRef]
28. Wang, W.; Zhang, X.; Jiang, R.; Ma, H. Field of view-independent detection of secondary mirror position errors in coaxial reflecting space telescopes using deep learning. *Appl. Opt.* **2024**, *63*, 9645–9653. [CrossRef]
29. Upton, R. Optical control of the advanced technology solar telescope. *Appl. Opt.* **2006**, *45*, 5881–5896. [CrossRef]
30. Chen, L.; Kanwal, S.; Lu, Y.; Zhang, D.; Chen, X.; Chen, J.; Wen, J. Broadband generation of accelerating polygon beams with large curvature ratio and small focused spot using all-dielectric metasurfaces. *Nanophotonics* **2022**, *11*, 1203–1210. [CrossRef]
31. Tang, T.; Kanwal, S.; Lu, Y.; Li, Y.; Wu, S.; Chen, L.; Qian, Z.; Xie, Z.; Wen, J.; Zhang, D. 3D nano-printed geometric phase metasurfaces enabling complex amplitude/phase manipulation and structured focal fields. *Sci. China Phys. Mech. Astron.* **2023**, *66*, 274202.
32. Howard, A.; Sandler, M.; Chu, G.; Chen, L.-C.; Chen, B.; Tan, M.; Wang, W.; Zhu, Y.; Pang, R.; Vasudevan, V.; et al. Searching for MobileNetV3. In *Proceedings of the 2019 IEEE/CVF International Conference on Computer Vision (ICCV)*; IEEE: New York, NY, USA, 2019; pp. 1314–1324.

Disclaimer/Publisher's Note: The statements, opinions and data contained in all publications are solely those of the individual author(s) and contributor(s) and not of MDPI and/or the editor(s). MDPI and/or the editor(s) disclaim responsibility for any injury to people or property resulting from any ideas, methods, instructions or products referred to in the content.